New Journal of Physics
The open access journal at the forefront of physics

Deutsche Physikalische Gesellschaft DPG
IOP Institute of Physics

Published in partnership with: Deutsche Physikalische Gesellschaft and the Institute of Physics

OPEN ACCESS

RECEIVED
30 October 2019

REVISED
9 January 2020

ACCEPTED FOR PUBLICATION
22 January 2020

PUBLISHED
14 February 2020

Original content from this work may be used under the terms of the Creative Commons Attribution 4.0 licence.

Any further distribution of this work must maintain attribution to the author(s) and the title of the work, journal citation and DOI.

PAPER

Realization of Weyl semimetal phases in topoelectrical circuits

S M Rafi-Ul-Islam, Zhuo Bin Siu, Chi Sun and Mansoor B A Jalil[1]

Department of Electrical and Computer Engineering, National University of Singapore, Singapore
[1] Author to whom any correspondence should be addressed.

E-mail: e0021595@u.nus.edu, elesiuz@nus.edu.sg and elembaj@nus.edu.sg

Keywords: topoelectrical circuit, circuit Laplacian, quantum tight-binding model, Weyl semimetal, impedance resonances, Green's function

Abstract

In this work, we demonstrate a simple and effective method to design and realize various Weyl semimetal (WSM) states in a three-dimensional periodic circuit lattice composed of passive electric circuit elements such as inductors and capacitors (LC). The experimental accessibility of such LC circuits offers a ready platform for the realization of not only various WSM phases but also for exploring transport properties in topological systems. The characteristics of such LC circuits are described by the circuit admittance matrices, which are mathematically related to the Hamiltonian of the quantum tight-binding model. The system can be switched between the Type-I and Type-II WSM phases simply by an appropriate choice of inductive or capacitive coupling between certain nodes. A peculiar phase with a flat admittance band emerges at the transition between the Type-I and Type-II Weyl phases. Impedance resonances occur in the LC circuits at certain frequencies associated with vanishing eigenvalues of the admittance matrix. The impedance readout can be used to classify the Type-I and Type-II WSM states. A Type-I WSM shows impedance peaks only at the Weyl points (WPs) whereas a Type-II WSM exhibits multiple secondary peaks near the WPs. This impedance behaviour reflects the vanishing and non-vanishing density of states at the Weyl nodes in the Type-I and Type-II WSM phases, respectively.

1. Introduction

Exotic topological phases of matter have emerged as one of the most exciting branches of condensed matter physics in the past decades due to their exceptional electronic properties [1–3]. Although gapped topological materials such as topological insulators [4–6], integer quantum Hall insulators [7, 8] and topological superconductors [9] have attracted a lot of attention, the physics of topological gapless materials [10] has recently gained more prominence due to their novel properties. A three-dimensional topological gapless system can be characterized by the nature of its band degeneracy points where two bands touch each other in momentum space. These band degeneracy points are classified as either Dirac [11] or Weyl points (WP) [12, 13] depending on their symmetries. Dirac points appear only when both time-reversal [14] and inversion symmetry [15] are conserved in a system. On the contrary, WPs emerge if either or both symmetries are broken. Although both types of band touching points appear and annihilate pair-wise, WPs are more robust against perturbations than Dirac points. One important class of topological system that hosts WPs are called Weyl semimetals (WSMs) [16–19]. WSMs disperse linearly in all three spatial directions in the vicinity of the WPs. Since the linear dispersion around the WPs can be described by the Weyl Hamiltonian involving all three Pauli matrices, small perturbations do not lift the energy degeneracy but only displace the WPs in momentum space. Besides fundamental properties such as the massless and chiral nature of the bulk carriers and large carrier mobility [20, 21], WSM states also exhibit unusual transport phenomena like the quantum anomalous Hall effect [22], large positive magnetoresistance [23], Klein tunnelling [24, 25], chiral anomaly [26, 27] and novel quantum oscillations [28, 29]. These exotic features and inherent robustness against disorder make WSMs promising candidate for future generation nanoelectronics, spintronics [30] and valleytronics [31] devices. WSMs can be

© 2020 The Author(s). Published by IOP Publishing Ltd on behalf of the Institute of Physics and Deutsche Physikalische Gesellschaft

further classified as Type-I and Type-II based on the tilt of the Weyl cones around the WPs [32, 33]. Type-I WSMs are marked by the existence of point-like iso-energy surfaces at the WPs, and the simultaneous presence of carriers with both signs of group velocities near the WPs [34, 35]. In contrast, in the Type-II WSM phase, potential energy terms dominate over the kinetic energy terms in the energy relation. This modifies the dispersion relation in such a way that only one sign of group velocity exists along certain directions near the WPs. Moreover, there is a finite density of states (DOS) at the WPs. When the kinetic and potential energy contribute equally, the transition between the Type-I and Type-II phases arises where one of the bands become completely flat with vanishing group velocity. This is the so-called Type-III [36] or Critical-type WSM phase [37]. However, realizing WSM states in condensed matter systems and tailoring their properties are experimentally challenging. For instance, carrier doping in WSMs may compromise the stability of the Weyl phases due to broken translational symmetry [38]. Additionally, it is usually difficult to achieve transitions between different topological WSM phases (Types-I, II, III) in a given material, and thus to form heterojunctions of WSMs of different phases [23, 39, 40]. There is hence a need for alternative platforms to realize gapless topological states. Researchers have studied various artificial systems such as photonic crystals [41], metamaterials [42, 43] and quantum resonators [44]. However, these methods all come with their own experimental complexities and limitations. Recently, topological states were realized in periodic electrical circuits consisting of inductors and capacitors (LC networks) known as topoelectrical (TE) circuits [36, 45]. Under the TE framework, many striking phenomena have been demonstrated such as the quantum spin Hall insulator state [46], magnet-less Floquet topological insulator state [47], topological photonic state [48], and edge modes in the SSH model [49]. A key advantage of electrical networks is the flexibility of experimental realization, as the circuits can be implemented even on simple printed circuit boards. Additionally, circuit parameters in electrical networks can be more readily adjusted and tuned, compared to lattice model properties of real materials.

In this paper, we demonstrate the realization of Type-I and Type-II WSM phases in a three-dimensional TE circuit network. We relate the admittance matrix of a TE circuit to the tight-binding Hamiltonian matrix of a condensed matter system. The resultant admittance band structure in a LC model resembles the energy dispersion [50]. The transition between Type-I and Type-II WSM phases can be readily effected by tuning the coupling between certain nodes. Moreover, we realize a distinct topological phase at the transition between the Type-I and Type-II phases, by isolating these nodes. This so-called Critical-type phase is characterized by the emergence of a flat admittance spectrum for one of the bands. We additionally derive the impedance spectrum and relate it to the circuit Green's functions [51]. The impedance spectra of the TE circuits corresponding to different WSM phases show significant differences. The Type-I WSM impedance spectrum is marked solely by distinctive peaks at the WPs. On the contrary, the Type-II WSM impedance dispersion exhibits not only impedance peaks at the WPs but also multiple secondary peaks along the tilt direction in wave-vector space. Finally, the intermediate Critical-type phase is characterized by a high impedance region between two WPs which signifies the flat dispersion of the electron or hole bands there. In short, TE circuits provide an accessible and tunable platform to design and model distinct topological phases and transitions in WSMs, while their impedance spectra provide a signature of the different phases.

2. Topoelectrical circuit model

Here, we consider a periodic (along all directions) LC circuit, shown in figure 1, which comprises of two sublattices A and B. In an AC circuit, the admittance Y of any two-terminal device component (resistor, capacitor, inductor etc) can be expressed as $Y = I_\alpha V_\alpha^{-1}$ where I_α and V_α are the current and the potential difference across the circuit component, respectively. In general, I_α and V_α are complex numbers [52]. By applying Kirchhoff's current law (KCL) at nodes A and B in the unit cell at $\vec{r} = (x, y, z)$ of the circuit model shown in figure 1, we have:

$$(\mathrm{i}\omega)^{-1} I^A_{x,y,z} = V^A_{x,y,z}(C_1 + C_2 - (\omega^2 L)^{-1} + 4C_n + 2C_{Bz} + 2C_y + 2C_{Az}) - C_1 V^B_{x,y,z} - C_2 V^B_{x-1,y,z} - C_y(V^B_{x,y+1,z} + V^B_{x,y-1,z}) - C_n(V^A_{x+1,y,z} + V^A_{x-1,y,z} + V^A_{x,y+1,z} + V^A_{x,y-1,z}) - C_{Az}(V^A_{x,y,z+1} + V^A_{x,y,z-1}), \quad (1)$$

$$(\mathrm{i}\omega)^{-1} I^B_{x,y,z} = V^B_{x,y,z}(C_1 + C_2 - (\omega^2 L)^{-1} + 4C_n + 2C_{Bz} + 2C_y + 2C_{Az}) - C_1 V^A_{x,y,z} - C_2 V^A_{x-1,y,z} - C_y(V^A_{x,y+1,z} + V^A_{x,y-1,z}) - C_n(V^B_{x+1,y,z} + V^B_{x-1,y,z} + V^B_{x,y+1,z} + V^B_{x,y-1,z}) - C_{Bz}(V^B_{x,y,z+1} + V^B_{x,y,z-1}), \quad (2)$$

where ω is the frequency of the alternating current, C_1 and C_2 are the intra- and inter-cell coupling capacitances along the x direction and C_y is the coupling along the y direction between lattice points on the same A/B sublattice. The lattice circuit model in the x–y plane is connected symmetrically with capacitors C_{Az} and C_{Bz}, respectively, between A–A and B–B sites of adjacent layers along the z axis. C_n denotes the next nearest lattice interaction between A–A or B–B sub-lattice nodes along both the x and y directions. The A and B lattice points

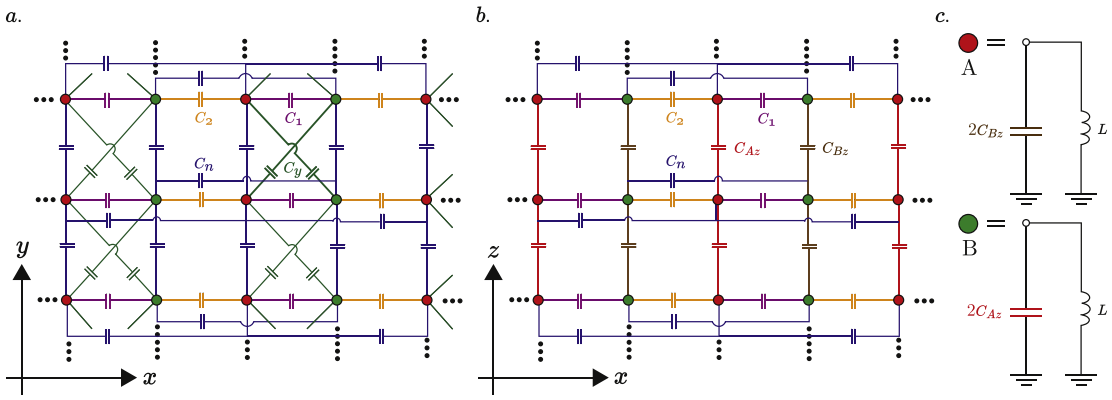

Figure 1. Illustration of a TE circuit lattice to realize various WSM phases. Periodic boundary conditions are considered along all directions. (a) The circuit representation in the x–y plane, where each A-type (red dot) node is connected to a B-type node (green dot) by C_1, and the repeating units are connected by C_2 in the x direction. All alternate lattice sites along the y direction are connected by C_y. Nodes of the same type are coupled to each other by C_n in the x–y plane. (b) The circuit representation in the x–z plane. All A–A couplings are capacitive in nature with magnitude C_{Az}, while the B–B coupling can be tuned to be in-phase (out-of-phase) with respect to the A–A coupling by selecting capacitive (inductive) hopping strengths C_{Bz} ($|L_B| = |(\omega^2 C_{Bz})^{-1}|$), respectively, along the z direction. (c) Additionally, all $A(B)$ nodes are connected to ground by common inductor L in parallel with capacitor $2C_{Bz}$ ($2C_{Az}$) respectively. The common inductor L determines not only the resonant frequency of the circuit but also the effective offset 'potential' of the TE circuit.

are grounded by capacitors $2C_{Bz}$ and $2C_{Az}$ respectively, and an additional inductance L that serves to adjust the offset 'potential'. Note that the capacitors C_{Bz} can be replaced by inductors L_B ($L_B = -(\omega^2 C_{Bz})^{-1}$) to switch the WSM phase of the circuit (see later). The schematic diagram of the various capacitive and inductive couplings in the LC circuit is depicted in figure 1. Using the Fourier transformation $\mathbf{V}(\vec{k}) = \sum e^{(i\vec{k}\cdot\vec{r})}\mathbf{V}(r)$, equations (1) and (2) can be expressed in momentum k space, in analogy to the tight binding (TB) approach in a crystal lattice model [53]. The relation between voltage and current distribution in k space can then be expressed in terms of the Laplacian matrix equation [36, 49]

$$\mathbf{i}(\vec{k}) = \mathbf{L}_{\mathrm{Weyl}}(\vec{k})\mathbf{v}(\vec{k}), \tag{3}$$

where $\mathbf{v}(\vec{k}) = [V^A(\vec{k}),\ V^B(\vec{k})]^T$ and $\mathbf{i}(\vec{k}) = [I^A(\vec{k}),\ I^B(\vec{k})]^T$ are the vectors representing the potential and current distribution at the A and B sublattice nodes in k space, respectively. $\mathbf{L}_{\mathrm{Weyl}}(\vec{k})$ denotes the admittance matrix (Laplacian matrix) which is analogous to the Hamiltonian in condensed matter physics [36], and can be expressed as

$$\begin{aligned}(i\omega)^{-1}\mathbf{L}_{\mathrm{Weyl}}(\vec{k}) = ((C_1 + C_2 + 2C_y - (\omega^2 L)^{-1} + 2C_n(1 - \cos k_x) + 2C_n(1 - \cos k_y) + (C_{Az} + C_{Bz})\\ \times (2 - \cos k_z))\sigma_0 - (C_1 + C_2\cos k_x + 2C_y\cos k_y)\sigma_x - C_2\sin k_x\sigma_y - (C_{Az} - C_{Bz})\cos k_z\sigma_z,\end{aligned} \tag{4}$$

where $(\sigma_x,\ \sigma_y,\ \sigma_z)$ are the Pauli matrices corresponding to the A/B sublattice pseudospin degree of freedom and σ_0 is the 2×2 identity matrix. The admittance spectrum, which corresponds to the energy dispersion in the quantum TB model [36], is obtained from the eigenvalues of $\mathbf{L}_{\mathrm{Weyl}}(\vec{k})/(i\omega)$ in equation (4):

$$E = d_0 \pm \sqrt{(C_1 + C_2\cos k_x + 2C_y\cos k_y)^2 + (C_2\sin k_x)^2 + (C_{Az} - C_{Bz})\cos k_z)^2}\,, \tag{5}$$

where $d_0 = C_1 + C_2 + 2C_y - (\omega^2 L)^{-1} + 2C_n(1 - \cos k_x) + 2C_n(1 - \cos k_y) + (C_{Az} + C_{Bz})(2 - \cos k_z)$. Here, the 'energy' E refers to the admittance (divided by $i\omega$) of the circuit. The energy spectrum is gapless at the charge neutrality point or WP in which the two eigenvalues of equation (5) are equal. This equality is satisfied by the following conditions

$$\sin k_x = \cos k_z = 0, \tag{6}$$

$$C_1 + C_2\cos k_x + 2C_y\cos k_y = 0. \tag{7}$$

Without loss of generality, we consider all capacitances and inductances as having non-negative values, $2C_y > (C_2 - C_1)$ and $C_1 + C_2 > 2C_y$. The solution set of equation (6) is then $(k_x,\ k_z) = \{(0,\ \pm\pi/2),\ (\pi,\ \pm\pi/2)\}$, which reduces equation (7) to

$$C_1 + \eta C_2 + 2C_y\cos k_y = 0, \tag{8}$$

where $\eta = 1$ for $(k_x,\ k_z) = (0,\ \pm\pi/2)$ and $\eta = -1$ for $(k_x,\ k_z) = (\pi,\ \pm\pi/2)$. However, for our parameter range, no real solution of k_y exists in the first Brillouin zone for $\eta = 1$. For $\eta = -1$, we obtain two pairs of WPs in k space which are located at $\vec{w}_\pm = (\pi,\ \pm\arccos(C_2 - C_1)/2C_y),\ \pm\pi/2)$. For $|(C_2 - C_1)| > 2C_y$, no band touching points exist. The type of WPs hosted by the Laplacian in equation (4), either Type-I or Type-II, depends

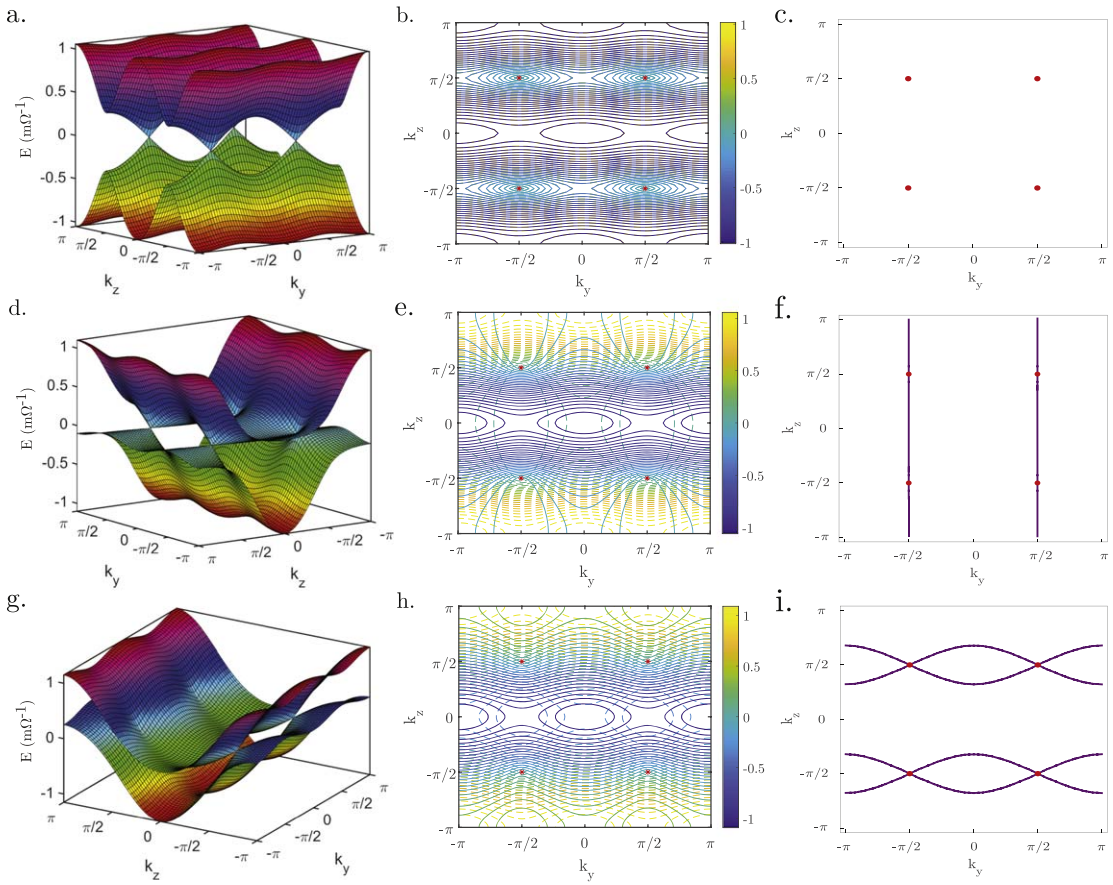

Figure 2. Admittance band analysis for TE circuit model for different WSM phases at resonant frequency with common parameters $C_1 = 0.716$ mF, $C_2 = 0.716$ mF, $C_y = 0.167$ mF, $C_n = 0$ mF and $L = 1$ mH, (a) 'Energy' (admittance) spectrum corresponding to Type-I WSM, with inductive B–B coupling along the z direction with parameters $C_{Az} = 0.5$ mF, $L_B = -\omega^{-2}C_{Az}^{-1}$ and $k_x = \pi$. (b) Iso-admittance contour plot of the upper and lower admittance bands of a Type-I WSM in (a), projected on the k_y–k_z plane. The red dots denote WPs around which the iso-admittance curves form closed admittance surfaces. (d) Flat admittance bands with two pairs of WPs for Critical-type WSM (transition phase between Type-I and Type-II WSM) with same parameters as (a) but with zero coupling between the B–B sites along the z axis. (e) Iso-admittance contour plot of the upper and lower admittance bands of a Critical-type WSM in (b), projected on the k_y–k_z plane. The upper band shows a zero energy contour line that connects two opposite WPs at $k_y = \pm\pi/2$. This denotes the flat band feature at the transition point of Type-I and Type-II WSM. (g) Admittance spectrum corresponding to Type-II WSM phase with capacitive coupling between B–B and A–A also sites along the k_z direction, $C_{Az} = 0.5$ mF, $C_{Bz} = 0.2$ mF and $k_x = \pi$. Both upper and lower bands show group velocity of the same sign around the WPs in contrast to the Type-I dispersion of (a), opposite velocities. (h) Iso-admittance contour plot of the admittance bands of a Type-II WSM in (g), projected on the k_y–k_z plane. Due to the hyperbolic dispersion of Type-II WSM, the iso-admittance contour lines do not enclose the WPs. However, the number and position of WPs have not changed with respect to Type-I and Critical-type WSM. (c), (f), (i) Constant admittance cross section at $E = 0$, for admittance spectra in (a), (d) and (g) for the Type-I, Critical-type and Type-II WSM, respectively. Type-I WSM hosts no states at the nodal energy. Critical-type WSM phase exhibits straight line bulk-like states between WPs. In Type-II WSM, electron and hole pockets emerge at Fermi energy which touches the WPs.

on the values of C_n, C_{Az} and C_{Bz}, which determine the d_0 term in equation (5). These parameters do not shift the WPs in the k-space but only modify the tilt of the Weyl dispersion cones. Figure 2 shows the evolution of the resonant admittance band structures and iso-admittance contour plots for different WSM phases. The resonant frequency is given by

$$\omega_r = (L(C_1 + C_2 + 2C_y + 4C_n - 2C_n(\cos k_x + \cos k_y) + (C_{Az} + C_{Bz})(2 - \cos k_z)^{-1/2}, \tag{9}$$

where ω_r corresponds to the frequency at which the σ-independent terms in the Hamiltonian vanish. As shown in figure 2(a), when the hopping parameters between the A and B nodes along the z direction have opposite signs, a Type-I WSM dispersion is obtained. In contrast, when the coupling between two similar sites along the z direction has the same signs, the WSM phase changes to Type-II (figure 2(g)). The Critical-type phase between two WSM phases is depicted in figure 2(d), corresponding to zero coupling between two adjacent B–B nodes along the z axis. As shown in figure 2(b), for the Type-I WSM phase, the constant admittance (iso-admittance) contour is a closed loop in the k_y–k_z plane that encompasses the WPs. In contrast, the iso-admittance contours for Type-II WSM are hyperbolic and connect the WPs with different chiralities, as shown in figure 2(h) for both energy bands. The contours for the transitional Critical-type phase between Type-I and Type-II WSMs are distinct from the other two types, as depicted in figure 2(e). For this phase, the WPs are connected by the zero-admittance contour lines for the electron (upper) band while for the hole (lower) admittance band, vanishing

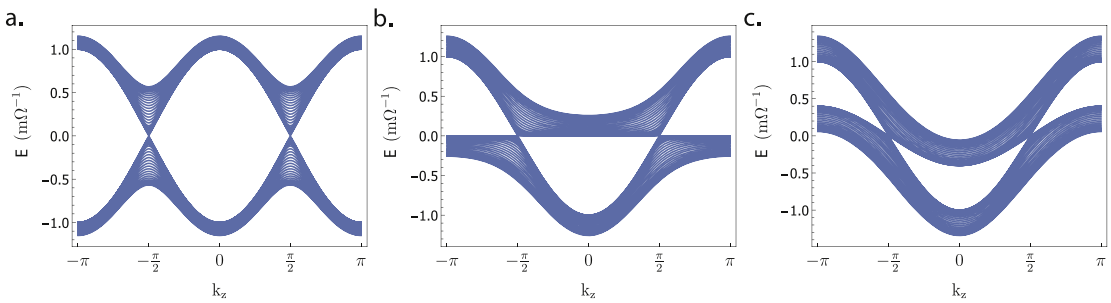

Figure 3. Numerical admittance dispersions for the Type-I, Critical-type and Type-II WSM phases of a LC circuit lattice network with 60 nodes and open boundary conditions along the y direction and periodic boundary conditions in the x and z directions. $C_1 = 0.716$ mF, $C_2 = 0.95$ mF, $C_y = 0.167$ mF, $C_n = 0$ mF, $L = 1$ mH and $k_x = \pi$. (a) Admittance spectrum as a function of k_z for $C_{Az} = -C_{Bz} = 0.5$ mF, with band degeneracy at two Type-I WPs. (b) Admittance spectrum for the Critical-type WSM with $C_{Az} = 0.5$ mF and $C_{Bz} = 0$ mF. There are zero-admittance states between the two WPs. (c) Admittance spectrum of the Type-II WSM system with $C_{Az} = 0.5$ mF and $C_{Bz} = 0.2$ mF. The value of the positive C_{Bz} is sufficiently large to tilt the two bands such that both will have group velocity of the same sign.

admittance is obtained for the rest of Brillouin zone along the k_z direction for a specific value of k_y that satisfies equation (7). Another method to classify the different WSM phases in the TE circuit model is by noting the existence of fintie DOS in the vicinity of WPs, as shown in figures 2(c), (f) and (i). In figure 2(c), there is zero DOS near WPs in the Type-I WSM where the B–B coupling along the z direction is comprised of an inductor L_B. In figure 2(f), for the transitional Critical-type WSM where there is zero coupling between nearest B sites, the WPs are linked by a single arc of bulk states. Finally, in the Type-II WSM where the B–B coupling along the z direction is comprised of a capacitor C_{Bz}, the resulting tilt of the admittance band gives raise to non-zero local DOS for electron and hole bands in the vicinity of WPs. These are clearly visible in figure 2(i), where there is finite DOS at the nodal admittance giving rise to the electron and hole pockets in the k_y–k_z plane.

3. Low admittance general Laplacian and classification

To further examine the properties of the Laplacian equation (4), we perform a linear expansion of the Laplacian near the band touching points in k space. The general form of the linear Laplacian can be expressed as

$$(\mathrm{i}\omega)^{-1}\mathbf{L}_{\mathrm{Weyl}}(\vec{q}) = (v_x q_x \sigma_y + \lambda v_y q_y \sigma_x + v_z q_z \sigma_z) + (t_x q_x + \lambda t_y q_y + t_z q_z)\sigma_0 + v_0 \sigma_0, \tag{10}$$

where $\vec{q} \equiv (q_x, q_y, q_z) = \vec{k} - \vec{w}_{\pm}$ is the small displacement from the WPs, $v_x = C_2$, $v_y = 2C_y \sin\theta$, $v_z = (C_{Az} - C_{Bz})$, $t_x = 0$, $t_y = 2C_n \sin\theta$, $t_z = (C_{Az} + C_{Bz})$, $v_0 = C_1 + C_2 + 2C_y - (\omega^2 L)^{-1} + 4C_n + 2C_n(1 - \cos\theta) + 2(C_{Az} + C_{Bz})$, $\theta = \arccos((C_2 - C_1)/2C_y)$ and $\lambda = \pm 1$ for the k and k' valleys respectively. v_0 is a constant 'potential' offset which can be tuned to zero or any other arbitrary value by varying the inductance L. The tilt of the Weyl dispersion cones along the k_i direction increases with $|t_i/v_i|$. The Weyl phases can be classified based on this ratio: Type-I with $|t_i/v_i| < 1$ $(i = x, y, z)$ (figure 3(a)), Type-II with $|t_i/v_i| > 1$ (figure 3(c)) and Type III with $|t_i/v_i| = 1$ (figure 3 (b)). In the vicinity of the WP, the slope of the dispersion cone, which represents the group velocity, has opposite (same) signs for opposite signs of q_z in a Type-I (Type-II) WSM, while at the transition value $|t_i| = |v_i|$, one of the electron or hole bands has zero group velocity and hence a flat dispersion relation, which corresponds to the Critical-type phase. From equation (10), the linearized admittance spectra of the two bands are given by

$$E = (t_x q_x + \lambda t_y q_y + t_z q_z) + v_0 + \chi A, \tag{11}$$

where $\chi = \pm 1$ for electron and hole bands respectively and $A = \sqrt{v_x^2 q_x^2 + v_y^2 q_y^2 + v_z^2 q_z^2}$. The group velocities of the upper and lower bands are expressed by $\vec{V}_g = \nabla_k E = \left(\chi \frac{v_x^2 q_x}{A}, \lambda t_y + \chi \frac{v_y^2 q_y}{A}, t_z + \frac{\chi v_z^2 q_z}{A}\right)$. In the vicinity of WPs ($q_x \to 0$, $q_y \to 0$, $q_z \to 0$), $\vec{V}_g$ can be further approximated to

$$(V_g^x, V_g^y, V_g^z) = (\chi C_2, 2(C_n + \chi C_y)\sin\theta, (C_{Az} + C_{Bz}) + \chi(C_{Az} - C_{Bz})). \tag{12}$$

As can be seen in equation (12), electrons and holes can propagate along the opposite or the same directions depending on the respective circuit parameters. In the x-direction, the velocity is purely determined by the kinetic term (coefficient of σ_i), and the particle and hole bands show opposite gradient with respect to q_x. However, for the y and z directions there is a combination of kinetic and potential terms (coefficient of σ_0 associated with the dispersion tilt) in the group velocity expressions. If the potential term dominates over the kinetic term along any direction, the upper and lower bands will have the same sign of group velocity resulting in

a Type-II WSM. Conversely, if the kinetic term dominates along all directions, then the two bands would exhibit group velocities of opposite signs (Type-I WSM). Let us consider the case where the tilt exists along the y direction. The corresponding velocities V_g^{y+} and V_g^{y-} will have the same signs if $|C_n| > |C_y|$, giving rise to Type-II WPs. Conversely, if $|C_n| < |C_y|$, we would obtain Type-I WPs, where the two admittance bands have opposite signs of admittance gradient along the y direction. At the critical coupling value $|C_n| = |C_y|$, the amplitudes of the potential and kinetic hopping terms along the y axis are equal. This corresponds to the Critical-type phase, with a flat hole band close to the WPs (with vanishing velocity V_g^{y-}), while the electron band retains a finite group velocity V_g^{y+}. Interestingly, the second-nearest hopping along the x axis via the coupling capacitance C_n does not contribute to the tilt in that direction (n.b. $t_x = 0$ in equation (10)), but rather contributes to the offset 'potential' term, which may also be adjusted by tuning the common inductor L.

Thus far in our analytical derivation, we have considered an infinite LC circuit in all three directions. For the numerical verification of our analytical predictions, we consider a nanoribbon geometry in a LC circuit model with a finite width of $l_y = 30$ unit cells in the y-direction, under open boundary conditions. Here, multiple sub-bands are present due to the quantum confinement along the y direction. We consider the evolution of the admittance dispersion through the different WSM phases as the B–B coupling parameter along the z-direction, C_{Bz}, is varied at a fixed $k_x = \pi$ and C_{Az}, as shown in figures 3(a)–(c). With an inductive coupling between two neighbouring B sites along the z direction, we have $C_{Bz} = -(\omega^2 L_B)^{-1}$. Any non-zero value of L_B will result in a dispersion tilt such that $|t_z/v_z| < 1$. The resulting Type-I WSM admittance dispersion is shown in figure 3(a). The dispersion relation consists of two symmetric bands touching each other at $k_z = \pm\pi/2$. The DOS at the WPs is zero and both signs of the admittance gradient are present in the vicinity of each WP. When the inductor L_B is replaced with a capacitor C_{Bz}, the B–B coupling C_{Bz} is in-phase with the corresponding A–A coupling, C_{Az}. In this case, both would have the same sign, so that $t_z > v_z$. In other words, for any positive value of C_{Bz}, $(C_{Az} + C_{Bz}) > (C_{Az} - C_{Bz})$ holds and so the Type-II WSM would result. This is reflected by the tipping over of the admittance bands into two asymmetric branches with respect to k_z (shown in figure 3(c)). The positions of the WPs are not shifted but the dispersion acquires a finite DOS at the nodal admittance—the line $E = 0$ cuts across multiple states in the E–k_z plot, spanning across the entire range of $-\pi < k_z < \pi$, in contrast to the Type-I WSM in figure 2(a) where the $E = 0$ line cuts across only the WP states. Finally, for the case of zero B–B coupling ($C_{Bz} = 0$), one of the admittance bands exhibits a flat zero admittance state between the two WPs ($-\pi/2 < k_z < \pi/2$) while the other shows zero admittance state elsewhere in the Brillouin zone, i.e. $|k_z| > \pi/2$, as shown in figure 3(b). This represents the intermediate Critical-type WSM system.

4. Impedance spectrum analysis

In the previous section, we presented the admittance dispersions for the different WSM phases of a TE model. In this section, we consider the impedance of a TE circuit and show that it offers an experimentally convenient way to distinguish the different topological phase of the TE circuit. The impedance readout of a TE circuit can be obtained simply by connecting a fixed current source to two arbitrary nodes in the circuit and measuring the potential difference between the nodes. This constitutes a more convenient measurement than a direct determination of the admittance dispersion relation of the circuit. Moreover, the comparatively large impedance readout (in the range of few Ω to kΩ) compared to the admittance readout (in the range of a few $m\Omega^{-1}$) provides a better measurement accuracy. We begin by analysing the mathematical significance of the impedance between any two lattice sites in a TE circuit. Consider a 2D TE circuit shown in figure 4 consisting of a finite number of nodes along the y direction, and having an infinite number of nodes along both the positive and negative x directions. Each node is capacitively coupled to its left and right neighbours by C_x, its upper and lower neighbours by C_y, and to the ground by a common grounding capacitance C. We also connect to every node an additional wire through which current may flow between the node and an external current supply. This wire is denoted as the dotted line with an arrow flowing into and out of the node, as shown in figure 4(b), and shall be referred to as the 'current wire' subsequently. We label the nodes by their (x, y) coordinates so that $V_{x,y}$ is the voltage at the node located at (x, y). The KCL at each node (except for those at the top and bottom rows) reads as

$$-\frac{I_{x,y}}{\mathrm{i}\omega} + CV_{x,y} = C_y(V_{x,y+1} + V_{x,y-1} - 2V_{x,y}) + C_x(V_{x-1,y} + V_{x+1,y} - 2V_{x,y}). \tag{13}$$

Let us first consider the case where $I_{x,y} = 0$ everywhere. Physically, this corresponds to leaving the current wire at each node unconnected to any current source or sink. Equation (13) with $I_{x,y} = 0$ then has a similar form to the Schrödinger equation for a quantum mechanical TB Hamiltonian [36], where the common grounding capacitance C is the analogue of the eigenenergy. More generally, the KCL for a TE circuit which has voltage nodes connected to common grounding capacitances C and current flowing through the current wires, can be written as

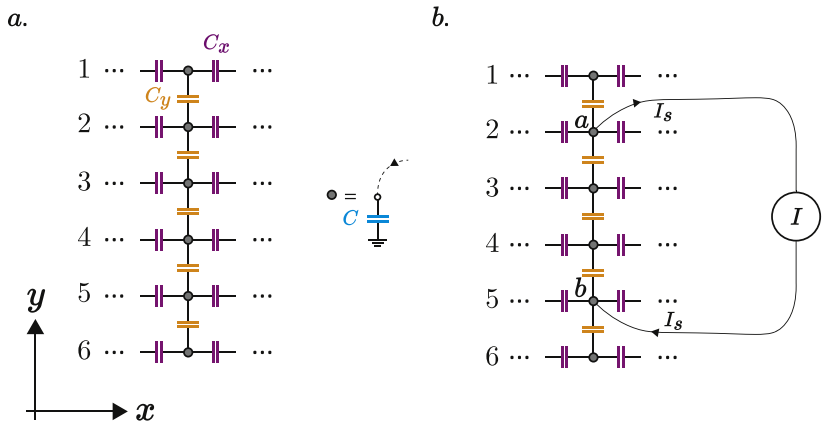

Figure 4. (a) Schematic of a TE circuit with a finite number of nodes along the y direction and infinite length along the x direction. The nodes are coupled to their left/right neighbours by C_x, upper/lower neighbours by C_y and the ground by C. Each node is connected to an additional wire through which current may flow in/out of the node. (b) The same circuit in (a) where we connect two arbitrary nodes to a current source.

$$-\frac{\mathbf{i}}{\mathrm{i}\omega} + C\mathbf{v} = \mathbf{H}\mathbf{v} \tag{14}$$

$$\Rightarrow \mathbf{i} = \mathrm{i}\omega(C - \mathbf{H})\mathbf{v} \equiv \mathbf{L}\mathbf{v}, \tag{15}$$

where $\mathbf{i}$ is the vector of currents flowing through the current wires at every node and $\mathbf{v}$ is the vector of voltages at every node. $\mathbf{H}$ is the matrix relating the voltages at the different nodes to one another, obtained by applying KCL at every node but excluding the contribution of the common grounding capacitance C, which is moved to left hand side of the equation (14). If $I_{x,y}$ is set to 0 everywhere, equation (14) becomes an eigenvalue equation in C and $\mathbf{v}$, as mentioned earlier. In particular, if $\mathbf{H}$ is a finite-sized matrix, then the system becomes equivalent to an infinite potential well system with a discrete eigenspectrum of C consistent with having $I_{x,y} = 0$ everywhere. In equation (15), we defined $\mathbf{L} \equiv \mathrm{i}\omega(C - \mathbf{H})$ where $\mathbf{L}$ is the TE analogue of the inverse of the Green's function $\mathbf{G}_{\mathrm{TB}}$ for a TB system with Hamiltonian $\mathbf{H}_{\mathrm{TB}}$, i.e. $\mathbf{G}_{\mathrm{TB}}^{-1} = (E - \mathbf{H}_{\mathrm{TB}})$. Let us consider the situation where the TE circuit is translationally invariant along the x direction, resulting in the form of $V(x, y) = V(y)\exp(\mathrm{i}k_x x)$. Equation (15) then reduces to

$$\frac{I_{x,y}}{\mathrm{i}\omega}\exp(-\mathrm{i}k_x x) = CV_y - C_y(V_{y+1} - V_{y-1} - 2V_y) + 2C_x V_y(\cos(k_x) - 1) \tag{16}$$

and the system is mathematically equivalent to a one-dimensional system with a k_x dependent 'on-site potential' $2C_x(\cos(k_x) - 1)$. Equation (16) can be schematically written as

$$\mathbf{i}_{(1)}\exp(-\mathrm{i}k_x x) = \mathbf{L}_{(1)}\mathbf{v}_{(1)}, \tag{17}$$

where the (1) subscript denotes a quasi one-dimensional system, where the effects of the infinite-length x direction have been incorporated as a k_x dependent on-site potential. In particular, for the nodes at $x = 0$, we have

$$\mathbf{v}_{(1)} = \mathbf{L}_{(1)}^{-1}\mathbf{i}_{(1)}. \tag{18}$$

We then consider the situation depicted in figure 4(b) where two nodes at $y = a$ and $y = b$ are connected to a current source supplying a current as I_{S} (the subscript 'S' denotes source), while the other nodes are left unconnected. This corresponds to setting $\mathbf{i}_{(1);a} = -\mathbf{i}_{(1),b} = I_{\mathrm{S}}$, $\mathbf{i}_{(1),c} = 0$, $c \neq \{a, b\}$. The resulting voltages at nodes a and b, $V_{a/b}$ can be read off from equation (18) as

$$V_a = \mathbf{L}_{(1);a,a}^{-1}I_{\mathrm{S}} - \mathbf{L}_{(1);a,b}^{-1}I_{\mathrm{S}} \tag{19}$$

$$V_b = \mathbf{L}_{(1);b,b}^{-1}(-I_{\mathrm{S}}) + \mathbf{L}_{(1);b,a}^{-1}I_{\mathrm{S}}, \tag{20}$$

where $\mathbf{L}_{(1);i,j}^{-1}$ is the ith row and jth column matrix element of $\mathbf{L}_{(1)}^{-1)}$. Denoting the potential difference across the current source as $\Delta V_{ab} = V_a - V_b$, the impedance across the current supply is given by $Z_{ab} = \Delta V_{ab}/I_{\mathrm{S}}$ so that

$$Z_{ab} = (\mathbf{L}_{(1);a,a}^{-1} + \mathbf{L}_{(1);b,b}^{-1} - \mathbf{L}_{(1);a,b}^{-1} - \mathbf{L}_{(1);b,a}^{-1}). \tag{21}$$

Letting N_y be the number of lattice sites along the y direction, $\mathbf{L}_{(1)}$ is then a $(N_y \times N_y)$ *Hermitian* matrix, the spectral decomposition of which is $A = \sum_i |a_i\rangle A_i \langle a_i|$ where $|a_i\rangle$ is the ith eigenvector and A_i its corresponding eigenvalue, i.e. $A|a_i\rangle = |a_i\rangle A_i$. Hence, any function $f(A)$ of the matrix can be expressed as $f(A) = \sum_i |a_i\rangle f(A_i)\langle a_i|$. Let us write the spectral decomposition of $\mathbf{H}_{(1)}$ as $\mathbf{H}_{(1)} = \sum_j |h_j\rangle c_j \langle h_j|$ with

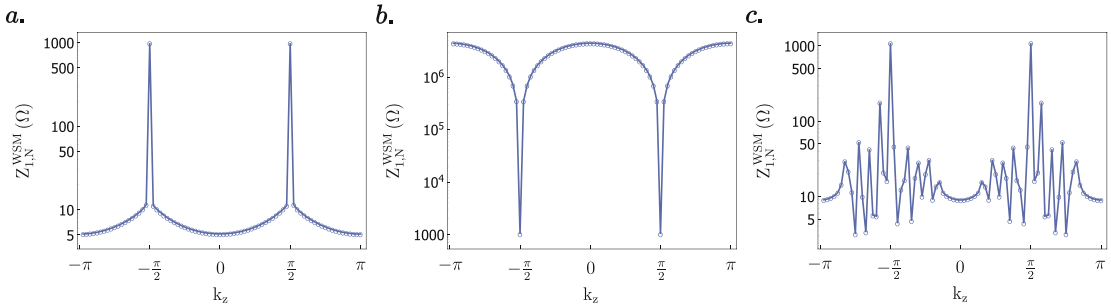

Figure 5. Impedance spectra for various Weyl phases at resonant frequency between the first and last nodes ($N = 60$) with $C_1 = 0.72$ mF, $C_2 = 0.95$ mF, $C_y = 0.167$ mF, $C_n = 0$ mF, $L = 1$ mH and $k_x = \pi$. (a) Resonant impedance behaviour for Type-I WSM network that shows large impedance peaks at the WPs. (b) In the impedance spectrum for Critical-type WSM system, the two WPs are marked by deep troughs even though their magnitude is comparable to the peak impedance value of Type-I WSM. However, the other points in k space show even larger impedance due to flat band nature at the transition phase. (c) Impedance spectrum for Type-II WSM system shows two primary peaks at the WPs and multiple secondary impedance peaks around the WPs due to the non-zero DOS in the vicinity of WPs arising from the electron and hole pockets.

$\mathbf{H}_{(1)}|h_j\rangle = |h_j\rangle c_i$. By definition $\mathbf{L}_{(1)} \equiv \frac{1}{\mathrm{i}\omega}(C - \mathbf{H}_{(1)})$, so $\mathbf{L}^{-1}$ has the spectral decomposition

$$\mathbf{L}_{(1)}^{-1} = \frac{1}{\mathrm{i}\omega}\sum_j \frac{|h_j\rangle\langle h_j|}{C - c_j} \tag{22}$$

and substituting the above into equation (21), we have

$$Z_{ab} = \frac{1}{\mathrm{i}\omega}\sum_j \frac{h_{j;a}^* h_{j;a} + h_{j;b}^* h_{j;b} - h_{j;a}^* h_{j;b} - h_{j;b}^* h_{j;a}}{C - c_j} \tag{23}$$

$$= \frac{1}{\mathrm{i}\omega}\sum_j \frac{(h_{j;a}^* - h_{j;b}^*)(h_{j;a} - h_{j;b})}{C - c_j} \tag{24}$$

$$= \frac{1}{\mathrm{i}\omega}\sum_j \frac{|h_{j;a} - h_{j;b}|^2}{C - c_j}, \tag{25}$$

where $h_{j;a}$ is the ath element of h_j. Equations (21) and (25) are the key formulae to evaluate the impedance between any two arbitrary points. When C is one of the eigenvalues of $H_{(1)}$ and provided that $|h_{j;a} - h_{j;b}|$ is not simultaneously zero, the current flowing through the current wires attached to the nodes will be nearly zero, leading to a sharp spike in the impedance Z_{ab}. This phenomenon is similar to that in quantum-dot (QD) systems [54, 55], in which a resonance occurs in the transmission across the system when the Fermi energy in the leads coincides with one of the discrete energy levels in the QD. Here C plays the role of the lead Fermi energy and c_j the discrete energy levels in the QD.

The impedance spectra across the whole circuit, i.e. between the first and last nodes ($N = 2n$) are plotted as a function of k_z at the resonant frequency for various WSM phases (see figure 5). Here, we consider $n = 30$ unit cells so that there are $N = 60$ alternating A and B lattice points. As can be seen in figure 5, the impedance distribution is symmetric about $k_z = 0$ for all types of WSM phases but assume different profiles for different phases. Figure 5(a) shows the impedance readout of a Type-I WSM TE circuit. The notable characteristic of the impedance spectrum is the presence of two clear peaks at the k points corresponding to the WPs in the k_z direction. These may be explained by considering equation (25) and figure 3(a). Figure 3(a) shows the hole and particle-like bands almost touching only at the WPs, where the admittance matrix is nearly zero. (The hole and particle bands do not actually touch due to the small band gap as a result of the finite width.) Equation (25) shows that the impedance between two points is dominated by the eigenvalues of the Laplacian matrix closest to $C = 0$, and inversely proportional to these eigenvalues. Thus, large impedance peaks are observed in the vicinity of WPs of Type-I circuit model. At k values away from the WPs, the eigenvalues of electron and hole bands have relatively large (non-zero) magnitudes, resulting in the decay of impedance readout (figure 5(a)). The impedance spectrum along k_z is plotted in figure 5(b) for Critical-type WSMs. As we have seen from figure 3(b), the electron and hole bands in the spectrum exhibit a flat band dispersion. The corresponding WPs are marked by two impedance minima, but the corresponding impedance value is large and of the same order of magnitude as that of the impedance peaks in Type-I WPs. At other k values between the WPs, the impedance exhibits much larger values by several orders of magnitude. The existence of large impedance over the whole of the Brillouin zone apart from the WPs is the direct consequence of the zero-admittance flat dispersion in the admittance spectrum. Finally, the resonant impedance characteristics of a Type-II WSM is illustrated in figure 5(c), which shows an

oscillatory response along the momentum direction that is parallel to the tilt direction (i.e. the k_z direction). The primary impedance peaks occur at $k_z = \pm\pi/2$, just as in the Type-I WSM system, but in addition there are multiple secondary peaks at other values of k_z. The emergence of these secondary peaks is due to the presence of eigenvalues with small magnitude of admittance, thus indicating the existence of finite DOS in the proximity of Type-II WPs. This is in line with the presence of hole and electron pockets as can be seen in the admittance dispersion for Type-II WSM shown in figure 3(c).

5. Conclusion

In conclusion, we have realized and characterized various WSM phases in the admittance dispersion of three-dimensional LC topoelectric circuit. The characteristics of such LC circuits are described by the circuit admittance matrices, which are analogous to the Hamiltonians of the quantum tight-binding model. The different phases of the circuit can be switched between one another by adjusting the magnitude and sign of the capacitive/inductive coupling in the circuit lattice. An intermediate Critical-type WSM phase with a flat admittance band emerges at the transition between the Type-I and Type-II phases. In practice, the impedance readout of the circuit can be used to classify its topological WSM phases. To show this, we numerically calculated the impedance between the terminal nodes using the Green's function analogy. The impedance spectra of the different WSM phases reveal different characteristics. The impedance spectrum of Type-I WSM shows peaks in the vicinity of WPs whereas a Type-II WSM exhibits multiple secondary peaks in addition to the main peaks at the WPs. This impedance behaviour reflects the vanishing and non-vanishing DOS at the WPs in the Type-I and Type-II WSM phases, respectively. The LC circuit model allows ready implementation of WSM phases using basic circuit elements. The accessibility and ease of fabrication of the LC circuits make them an ideal platform for the design and characterization of topological WSM states and their transport properties.

Acknowledgments

We would like to acknowledge MOE Tier I (NUS Grant No. R-263-000-D66-114), MOE Tier II MOE2018-T2-2-117 (NUS Grant No. R-398-000-092-112) grants and NRF-CRP12-2013-01 (NUS Grant No. R-263-000-B30-281) for financial support.

ORCID iDs

S M Rafi-Ul-Islam https://orcid.org/0000-0002-2275-8889
Zhuo Bin Siu https://orcid.org/0000-0002-7056-937X
Mansoor B A Jalil https://orcid.org/0000-0002-9513-8680

References

[1] Chiu C-K, Teo J C, Schnyder A P and Ryu S 2016 *Rev. Mod. Phys.* **88** 035005
[2] Goldman N, Budich J C and Zoller P 2016 *Nat. Phys.* **12** 639
[3] Senthil T 2015 *Annu. Rev. Condens. Matter Phys.* **6** 299
[4] Moore J E 2010 *Nature* **464** 194
[5] Chen Y *et al* 2009 *Science* **325** 178
[6] Rechtsman M C, Zeuner J M, Plotnik Y, Lumer Y, Podolsky D, Dreisow F, Nolte S, Segev M and Szameit A 2013 *Nature* **496** 196
[7] Kane C L and Mele E J 2005 *Phys, Rev. Lett.* **95** 146802
[8] Bernevig B A, Hughes T L and Zhang S-C 2006 *Science* **314** 1757
[9] Qi X-L and Zhang S-C 2011 *Rev. Mod. Phys.* **83** 1057
[10] Xu S-Y *et al* 2015 *Science* **347** 294
[11] Abanin D A, Novoselov K S, Zeitler U, Lee P A, Geim A K and Levitov L S 2007 *Phys. Rev. Lett.* **98** 196806
[12] Lu L, Wang Z, Ye D, Ran L, Fu L, Joannopoulos J D and Soljačić M 2015 *Science* **349** 622
[13] Xiao M, Lin Q and Fan S 2016 *Phys. Rev. Lett.* **117** 057401
[14] Chirolli L, de Juan F and Guinea F 2017 *Phys. Rev.* B **95** 201110
[15] Kim Y, Wieder B J, Kane C and Rappe A M 2015 *Phys. Rev. Lett.* **115** 036806
[16] Burkov A and Balents L 2011 *Phys. Rev. Lett.* **107** 127205
[17] Lv B *et al* 2015 *Phys. Rev.* X **5** 031013
[18] Xu S-Y *et al* 2015 *Science* **349** 613
[19] Huang S-M *et al* 2015 *Nat. Commun.* **6** 7373
[20] Rüßmann P *et al* 2018 *Phys. Rev.* B **97** 075106
[21] Shekhar C *et al* 2015 *Nat. Phys.* **11** 645
[22] Yang K-Y, Lu Y-M and Ran Y 2011 *Phys. Rev.* B **84** 075129
[23] Li P, Wen Y, He X, Zhang Q, Xia C, Yu Z-M, Yang S A, Zhu Z, Alshareef H N and Zhang X-X 2017 *Nat. Commun.* **8** 2150
[24] Orien T, Diez M and Beenakker C 2016 *Phys. Rev. Lett.* **116** 236401

[25] Yesilyurt C, Tan S G, Liang G and Jalil M B 2016 *Sci. Rep.* **6** 38862
[26] Huang X *et al* 2015 *Phys. Rev.* X **5** 031023
[27] Zyuzin A and Burkov A 2012 *Phys. Rev.* B **86** 115133
[28] Potter A C, Kimchi I and Vishwanath A 2014 *Nat. Commun.* **5** 5161
[29] Klotz J *et al* 2016 *Phys. Rev.* B **93** 121105
[30] Žutić I, Fabian J and Sarma S D 2004 *Rev. Mod. Phys.* **76** 323
[31] Schaibley J R, Yu H, Clark G, Rivera P, Ross J S, Seyler K L, Yao W and Xu X 2016 *Nat. Rev. Mater* **1** 16055
[32] Liu H, Sun J-T and Meng S 2019 *Phys. Rev.* B **99** 075121
[33] Huang L *et al* 2016 *Nat. Mater.* **15** 1155
[34] Xu N *et al* 2016 arXiv:1604.02116
[35] Yan M *et al* 2017 *Nat. Commun.* **8** 257
[36] Rafi-Ul-Islam S, Siu Z B and Jalil M 2019 arXiv:1908.03642
[37] Liu G, Jin L, Dai X, Chen G and Zhang X 2018 *Phys. Rev.* B **98** 075157
[38] Berke C, Michetti P and Timm C 2018 *New J. Phys.* **20** 043057
[39] Wu Y, Mou D, Jo N H, Sun K, Huang L, Bud'Ko S, Canfield P and Kaminski A 2016 *Phys. Rev.* B **94** 121113
[40] Belopolski I *et al* 2016 *Phys. Rev.* B **94** 085127
[41] Bonaccorso F, Sun Z, Hasan T and Ferrari A 2010 *Nat. Photonics* **4** 611
[42] Schurig D, Mock J, Justice B, Cummer S A, Pendry J B, Starr A and Smith D 2006 *Science* **314** 977
[43] Valentine J, Zhang S, Zentgraf T, Ulin-Avila E, Genov D A, Bartal G and Zhang X 2008 *Nature* **455** 376
[44] Oonnell A D *et al* 2010 *Nature* **464** 697
[45] Imhof S *et al* 2018 *Nat. Phys.* **14** 925
[46] Albert V V, Glazman L I and Jiang L 2015 *Phys. Rev. Lett.* **114** 173902
[47] Tymchenko M and Alù A 2016 *2016 10th Int. Congress on Advanced Electromagnetic Materials in Microwaves and Optics (METAMATERIALS)* (Piscataway, NJ: IEEE) pp 373–5
[48] Li Y, Sun Y, Zhu W, Guo Z, Jiang J, Kariyado T, Chen H and Hu X 2018 *Nat. Commun.* **9** 4598
[49] Lee C H, Imhof S, Berger C, Bayer F, Brehm J, Molenkamp L W, Kiessling T and Thomale R 2018 *Commun. Phys.* **1** 39
[50] Bracewell R N and Bracewell R N 1986 *The Fourier Transform and its Applications* vol 31999 (New York: McGraw-Hill)
[51] Wu F-Y 2004 *J. Phys. A: Math. Gen.* **37** 6653
[52] Boylestad R L, Nashelsky L and Li L 2002 *Electronic Devices and Circuit Theory* vol 11 (Englewood Cliffs, NJ: Prentice Hall)
[53] Reich S, Maultzsch J, Thomsen C and Ordejon P 2002 *Phys. Rev.* B **66** 035412
[54] Ma M, Jalil M B A and Tan S G 2013 *Ann. Phys.* **330** 95
[55] Ma M, Jalil M, Tan S and Koh D 2011 *Eur. Phys. J.* B **82** 37